Interplay of electrode geometry and bias on charge transport in organic heterojunction gas sensors

Abhishek Kumar, Rita Meunier-Prest, Eric Lesniewska, Marcel Bouvet

Graphical abstract

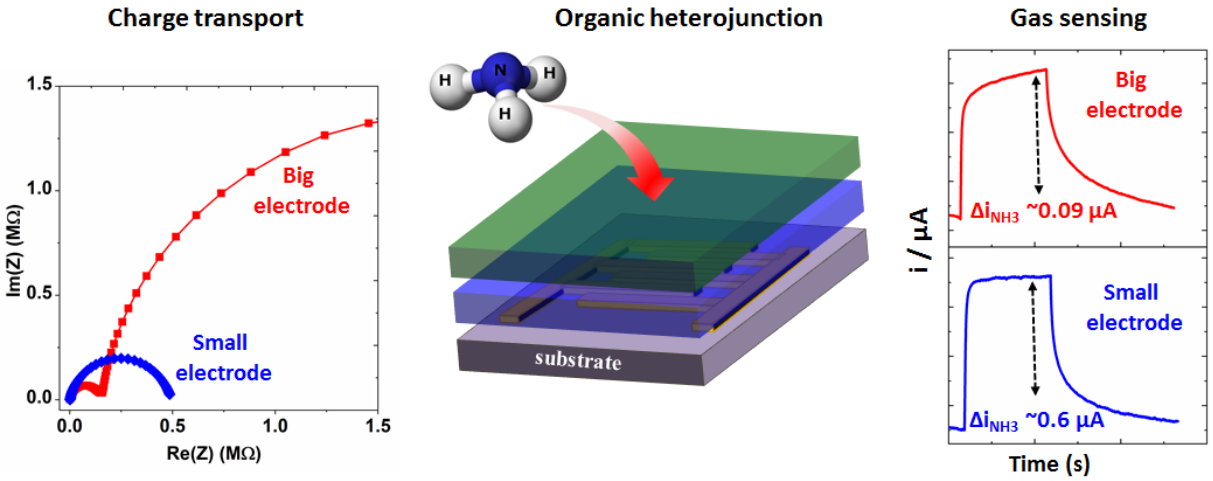

Interplay of electrode geometry and bias on charge transport in organic heterojunction gas sensors

Abhishek Kumar[1]*, Rita Meunier-Prest[1], Eric Lesniewska[2], Marcel Bouvet[1]*

[1]*Institut de Chimie Moléculaire de l'Université de Bourgogne, UMR CNRS 6302, Université Bourgogne Franche-Comté, 9 Avenue Alain Savary, Dijon Cedex 21078, France*

[2]*Laboratoire Interdisciplinaire Carnot de Bourgogne (LICB), UMR CNRS 6303, Université Bourgogne Franche-Comté, 9 avenue Alain Savary, 21078 Dijon cedex, France*

Email addresses and ORCID number of authors (corresponding authors emails are marked with asterisk)

*abhishek.Kumar@u-bourgogne.fr (ORCID no. 0000-0002-4306-9644)

rita.Meunier-Prest@u-bourgogne.fr (ORCID no. 0000-0001-5597-3879)

eric.lesniewska@u-bourgogne.fr (ORCID no. 0000-0002-8027-7223)

*marcel.bouvet@u-bourgogne.fr (ORCID no. 0000-0002-2272-6633)

Abstract: Modulation of charge transport in an organic heterojunction sensor is a promising strategy to enhance its gas sensing properties. Herein, a heterostructure consisting of a bilayer assembly of perfluorinated copper phthalocyanine and lutetium bis-phthalocyanine is investigated for ammonia sensor development in two different electrode geometries and in a wide range of applied bias. The microstructure of the heterostructure retains the bulk electronic and structural properties of the individual components and shows granular distribution of phthalocyanine crystallites on the surface. The charge transport of the heterojunction devices depends on the electrode geometry and the applied bias. Notably, interfacial charge transport gets faster, while bulk charge transport remains constant with increasing bias in both devices. But, the small gap between the electrodes fastens the bulk and the interfacial charge transport by 75 and 5 times, respectively, compared to the big gap electrodes. The implication of faster charge transport in the small gap electrodes-based sensor is demonstrated on its ammonia sensing properties, exhibiting higher response and shorter response time. Moreover, the response of the sensor exponentially increases with increasing bias. The high sensitivity and stability of the sensor at different relative humidity make it a suitable NH_3 sensor for real environment applications.

Keywords: Organic heterojunction, Phthalocyanine, Gas sensor, Impedance spectroscopy, Molecular semiconductor

---

1. Introduction

The research interests in gas sensors have witnessed tremendous growth in the diverse areas of air quality control, industrial emission monitoring and healthcare diagnostic [1-3]. Conventionally, metal oxides [4], carbon nanomaterials [5], conducting polymers [6] and molecular semiconductors [7] were employed as sensing materials. In these materials, different structural engineering were performed to improve the sensor performances such as sensitivity, selectivity, limit of detection and operational stability. A new trend has emerged in recent years for the sensing materials engineering, in which the conventional materials are being combined in heterostructure configurations. The strategy is promising to improve the metrological benchmarks of gas sensors for meeting the requirements of new application areas in healthcare and Internet of Things (IoT) [8, 9], besides overcoming the existing limitations of selectivity and room temperature operation. Metal oxide semiconductors have been associated among each other or with the varieties of 2D materials like transition metal dichalcogenides, Mxenes and graphene to develop heterostructure sensing materials [10]. Chemiresistor gas sensors based on these heterostructures have shown high sensitivity and selectivity for redox gases [11-15]. Moreover, these sensors exhibited a synergic enhancement in the sensing properties from the either constituent of the heterostructures. Despite displaying excellent sensing properties, the synthesis and film processing of inorganic heterostructures remain challenging, which often involve complex hydrothermal synthesis and mass loading by solution cast, causing poor reproducibility in the sensor measurements.

Organic heterostructures have found increasing interests in gas sensors development, especially those based on π-conjugated molecular semiconductors, such as Metal Phthalocyanines (MPc) and Metal Porphyrins (MP) [16]. The main rationale behind using organic heterostructures in gas sensors is ascribed to the organic heterojunction effect, causing accumulation of mobile charge carriers (electron (e^-) and hole (h^+)) at the organic/organic

interface [17]. It results in the enhancement of interfacial conductivity [18] that can be exploited to fasten the charge transfer during gas-sensing material interaction. MPc and MP are ideal choices for heterostructures development because their semiconducting and electronic properties can be modulated through maneuvering their molecular structure. Such molecular engineering can be performed by replacing central metal atom [19], attaching electron donor and/or acceptor substituents [20, 21] and interlinking macrocyclic units into extended polymeric network [22]. Organic field-effect transistors (OFET), employing MPc-based heterostructures were reported to exhibit high sensitivity, linear response and detection limit down to 250 ppb towards NO_2 at room temperature [23, 24]. Besides OFET sensors, we reported a two-terminal gas sensing transducer "Molecular Semiconductor-Doped Insulator" (MSDI) heterojunction, utilizing a bilayer heterostructure assembly of organic semiconductors, such that the layer close to the electrodes is low conducting, while the one above it is high conducting [25]. Such assembly facilitates the interfacial charge transport during the device operation [26]. Different MPc-based bilayer heterostructures were investigated in MSDI device design for ammonia sensing [27-29]. In majority of these sensors, lutetium bis-phthalocyanine ($LuPc_2$) was used as top layer because of its high conductivity [30]. Other than $LuPc_2$, porphyrin-tapes were also used as high conducting materials in such heterostructures exhibiting high sensitivity (LOD 228 ppb) to NH_3 [31].

In addition to sensing material engineering by heterostructure formation, electrode geometry is also a key parameter, which influences the performances of gas sensors [32]. Interdigitated electrodes (IDE) are commonly used in gas sensors because they allow a large electrode-sensing film contact, facilitating efficient charge transport during sensor operation. Previous studies on metal oxides-based chemiresistors have shown that the width of the digits and the gap between them influence gas sensitivity [33]. For instance, NO_2 sensing studies on SnO_2 chemiresistors having gap between the electrodes in the range of 1 to 30 µm were

investigated. It revealed that sensors with small gap between electrodes benefited from higher sensitivity and reliable response at low NO_2 concentration, while sensors with large gap between the electrodes exhibited better sensitivity at high NO_2 concentration [34]. The advantages of narrow gap electrodes in the gas sensors were also highlighted by Gardner et al., reporting improved stability of the sensor response under temperature variation and long-term ageing [35]. The effect of gap between electrodes in the range of 0.1 to 1.5 µm on NO_2 sensing properties of WO_3 thin film sensors was reported, exhibiting an exponential increase in the sensitivity as gap decreases from 0.8 to 0.1 µm [36]. This behavior was attributed to the lowering in grain boundaries resistance during the charge conduction, as smaller number of WO_3 grains remained between the electrodes, when gap between them decreased. Elsewhere, the effect of electrode geometry on NO_2 sensing properties of lead phthalocyanine chemiresistors was studied [37], reporting the effect of electrode gap on the sensors response time and sensitivity. Recently, the effect of fractal shapes of electrode geometry on the gas sensor performances was reported [38]. In this study, the fractal shape (Hilbert-piano shape)-based sensor displayed higher sensitivity to nitrogen oxide, compared to interdigitated electrode-based sensor. Higher sensitivity of the fractal shaped electrode-based sensor was attributed to the strengthening of the electric field lines at the sharp corner and curvature present in these electrodes. These corners/curvatures behave like a hot spot or a preferential adsorption site for gas molecules.

Although these works clearly established the important role played by the electrode geometry on the sensors performances, they do not provide a direct experimental evidence of charge transfer variations as the gap between the sensor electrodes changes. This phenomenon is crucial to understand because it ultimately determines the sensitivity and response kinetics of the sensors. Moreover, the previously reported works were performed only on conventional chemiresistors, while such studies of electrodes gap effect on the heterojunction sensor

performances have not been reported. Therefore, it necessitates a mechanistic study of electrodes gap effect on the heterojunction sensors performances, which are finding increasing research interests in gas sensors development.

In this endeavor, the present work investigates the effect of electrode geometry in MPc-based organic heterojunction sensors on its NH_3 sensing properties and provides a direct experimental evidence of variations in charge transfer between the electrodes, as gap between them changes. Our strategies involve microstructural characterizations of Cu(F_{16}Pc)/$LuPc_2$ heterostructure sensing film, followed by in-depth charge transport assessment by impedance spectroscopy, which are finally correlated to the gas sensing properties of the heterojunction sensors. The key novelty aspect of this work is to unravel the variations in bulk and interfacial charge transport in the heterostructure induced by changing the electrode geometry and their implication on the sensor performances, such as sensitivity, response/recovery kinetics and stability. Thus, the manuscript reports a significant advancement from the current state-of-art in the organic heterojunction gas sensors.

2. Experimental

2.1. **Reagents and materials synthesis**

The precursor compounds for Cu(F_{16}Pc) and $LuPc_2$ synthesis, including tetrafluorophthalonitrile, copper(II) chloride, lutetium acetate trihydrate ($Lu(OAc)_3$. $3H_2O$), were procured from Sigma-Aldrich and were used without any additional purification. o-phthalonitrile was purchased from Merck and was recrystallized in methanol. Solvents used in the synthesis, such as dimethylformamide, tetrahydrofuran, chloroform, ethanol and acetone were of analytical grade and were purchased from Merck. Cu(F_{16}Pc) and $LuPc_2$ were synthesized based on a previously reported procedure, details of which are described in the supporting information.

2.2. Material characterizations

The UV-Vis spectra of $LuPc_2$ and Cu(F_{16}Pc) thin films were obtained using a Varian's Cary®50 spectrophotometer, equipped with Xenon flash lamp as an excitation source in the range of 250-900 nm. Surface topography of Cu(F_{16}Pc)/$LuPc_2$ heterostructure film coated on glass was evaluated by AFM imaging, performed on a Bruker Icon-2 AFM equipment in nanoDMA peak-force tapping mode. Scan of the surface was performed using a silicon probe (ScanAsyst, AIR-HR) (spring constant: 0.4N/m, tip radius: 2 nm) at a peak-force frequency of 2 kHz and at amplitudes in the range of 25–75 nm. Thin films of $LuPc_2$, Cu(F_{16}Pc) and Cu(F_{16}Pc)/$LuPc_2$ bilayer coated on glass were characterized by XRD, using a PANanalytical X'pert MPD diffractometer at room temperature in 2θ range of 5–80°. The incident X-ray source was based on Cu-K_α (λ = 1.5418 Å).

2.3. Sensor development, characterizations and NH_3 sensing

Two different IDE geometries of ITO were patterned lithographically on a (1 × 1) cm^2 glass support as shown in Fig. 1a and 1b. In one case, 16 digits of ITO were patterned, in which the width of each digit and the gap between the two neighboring digits were 75 µm. The length and the height of each digit were 5.15 mm and 50 nm, respectively. In the other case, 125 digits of relatively smaller size (length: 2.5 mm, height: 20 nm) were patterned on glass substrate, in which the width of each digit and the gap between the two neighboring digits were 10 µm. The aforementioned IDEs will be referred as "big electrode" and "small electrode" hereinafter in the manuscript. The heterojunction sensors were fabricated by depositing sequentially 50 nm each of Cu(F_{16}Pc) and $LuPc_2$ thin films in a bilayer configuration (Fig. 1c) on the two different geometries of IDE, in a UNIVEX 250 thermal evaporator in secondary vacuum (ca. 1×10^{-6} mbar) and at a rate of 0.8 Å/s. The sublimation temperature of Cu(F_{16}Pc) and $LuPc_2$ was recorded in the range of 302–310°C and 405–414°C, respectively. The electrical properties of the heterojunction devices were characterized by I-V measurements, using Keithley electrometer (6517b) in the applied voltage range of -10 to +10 V with a step of 0.1 V, at room

temperature (20-22°C). The charge transport in the heterojunction devices was studied by impedance spectroscopy on a Solartron SI 1260 impedance analyzer integrated with SMART software. The measurements were performed in the frequency range of 10 Hz to 10 MHz at different applied DC (0 to 10 V) and AC bias (0.05 to 0.5 V). The experimental impedance data were fitted using Zview software through relevant circuits design and different charge transport parameters were obtained.

Ammonia sensing studies were performed on a homebuilt workstation, which detailed configurations and operation have been described in our recent work [39]. Briefly, there are three interconnected fluidic lines for the calibrated gas flow of NH_3, synthetic air and water vapor, which are also connected to the sensor test chamber of size 8 cm^3. The source of NH_3 (985 ppm, mol/mol) and synthetic air was commercial gas cylinders (Air Liquide), while humidity was in-house produced through a humidity generator, which was continuously calibrated by a commercial humidity sensor (HMT-100, Vaisala). The desired concentration of NH_3 and RH level in the test chamber were obtained through control of the opening and closing of the mass flow controllers in each fluidic line. The total flow in the sensor test chamber was maintained at 0.5–0.55 NL min^{-1}. Ammonia sensing was performed by alternate exposure and recovery periods of 10 or 1 min and 15 or 4 min, respectively. The sensing measurements were made at different bias in the range of 0.25 to 5 V and RH levels in the range of 10 to 70%. All sensing experiments were performed at room temperature (20-22°C).

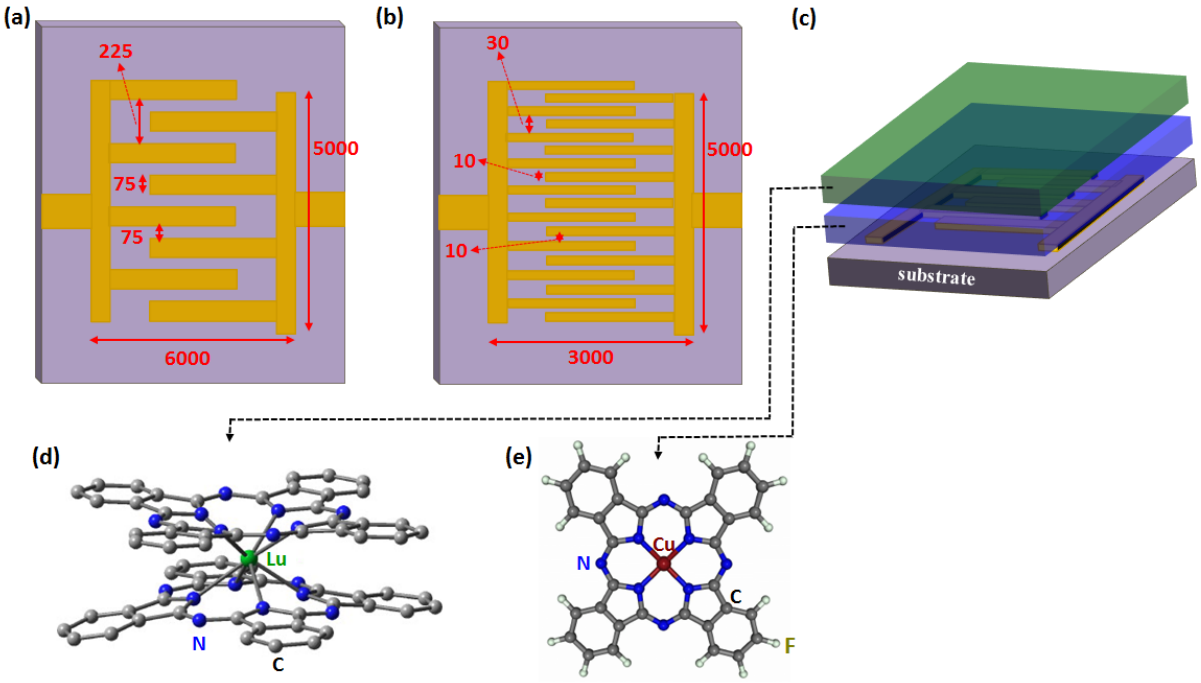

Figure 1: *Schemes of the two different IDE geometries based on the big electrode (a) and the small electrode (b). Dimensions are in µm. The scheme of Cu(F_{16}Pc)/$LuPc_2$ bilayer heterojunction sensors with a thickness of 50 nm of each layer (c). The molecular structure of $LuPc_2$ and Cu(F_{16}Pc) is shown in the image panels (d) and (e), respectively.*

3. Results and discussions

3.1. Microstructural characterizations of heterostructure

Fig. 2a depicts UV-Vis absorption spectrum of Cu(F_{16}Pc)/$LuPc_2$ bilayer and its comparison with the respective spectra of Cu(F_{16}Pc) and $LuPc_2$ thin films. The individual spectra of Cu(F_{16}Pc) and $LuPc_2$ exhibit the characteristics Q-band at 654 nm and 669 nm and B-band at 364 nm and 320 nm, respectively, of phthalocyanines. The origin of Q and B bands are associated to the electronic transitions from π to π* (HOMO to LUMO) and a_{2u} and b_{1u} (low lying orbitals) to π*, respectively [40]. An additional intense band at 788 nm appears in Cu(F_{16}Pc) spectrum, which is representative of this material and is called as charge transfer band. It originates from the charge transfer exciton state, formed by the edge to edge interaction between adjacent molecules in the thin film [41]. Moreover, the spectrum of $LuPc_2$ displays a

unique band at 466 nm, which is characteristic to the radical nature of the molecule [42]. The bilayer spectrum reveals a superposition of the absorption bands of Cu(F_{16}Pc) and $LuPc_2$, highlighting that constituents of the heterostructure retain their bulk electronic properties. Nonetheless, a slight hypsochromic shift in each absorption band is noted, which can be attributed to formation of H-aggregates by face-to-face interaction between the two macrocycles in the thin film [27]. The strong intermolecular interactions in the thin films of Cu(F_{16}Pc) and in the bilayer heterostructure suggest local organization in the films, which was confirmed from XRD measurements (Fig. S1). The high intensity and sharp reflection peak of Cu(F_{16}Pc) film confirm its crystalline nature, while low intensity and broad reflection peaks of $LuPc_2$ reveal amorphous nature of the film. The XRD profile of the heterostructure film presented intermediate features, suggesting that the crystallites of Cu(F_{16}Pc) in the sublayer provide a template for the organized growth of $LuPc_2$ over them [43].

The surface topography of the heterostructure film was investigated by AFM imaging, which revealed coverage of the surface with the granular crystallites of the macrocycles (Fig. 2b). However, two distinct features of the grain distribution are evident on the surface, which are also depicted in the surface-height variation profile of the selected line-scan (Fig. 2c). In one phase, there is a homogeneous distribution of closely packed grains of average size ca. 40 nm and of surface roughness ca. 4 nm. In the other phase, there is a non-homogeneous distribution of the larger size grains of average size ca. 85 nm and surface height ca. 50 nm. Moreover, there is also agglomeration of these bigger size grains, forming a few hundred nm wide clusters, depending on the number of grains involved. The granular topographical feature of MPc film was previously reported [44] and the evolution of the larger size grains is attributed to the post-deposition surface migration, causing coalescence among high surface energy grains of the macrocycles. The magnified AFM image (Fig. S2) of the heterostructure film shows the presence of a few surface pores, which sizes vary between 20 nm and 75 nm.

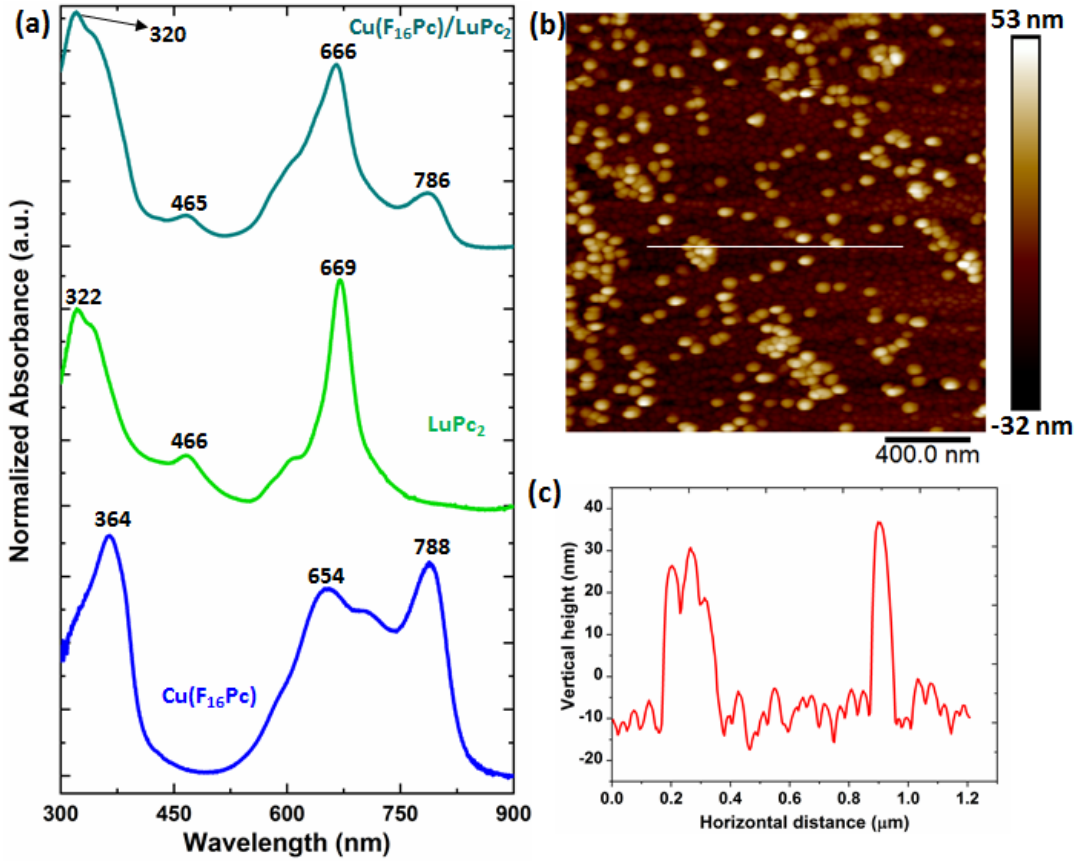

Figure 2: *Comparison of UV-Vis absorption spectra of thin films of Cu(F_{16}Pc), $LuPc_2$ and Cu(F_{16}Pc)/$LuPc_2$ bilayer heterostructure coated on glass substrate (a). AFM image (b) and surface height variation of Cu(F_{16}Pc)/$LuPc_2$ bilayer film coated on glass substrate (c).*

3.2. Electrical properties of heterojunction

The electrical nature of the MSDI heterojunction devices was studied at first by recording I-V profile in the potential range of -10 V to +10 V. It reveals a non-linear increase of current as a function of the applied potential for both devices, which is typical for non-ohmic charge transport (Fig. 3). Such I-V profile is a characteristic feature of MSDI heterojunction device, which originates from the accumulation of mobile charge carriers, e^- and h^+, at the interface of Cu(F_{16}Pc) and $LuPc_2$ in the heterostructure [26]. However, a clear difference in the I-V profiles is noted. The device with small electrode displays ca. 700 µA current at 10 V, which is ca. 15.5-times higher than the respective current of the device with big electrode. Moreover, the apparent energy barrier (U_{th}), which is estimated by the extrapolation of the

tangent to the I-V curve at higher bias on the abscissa, is larger in the small electrode-based device (5.4 V) compared to the big electrode-based device (3.1 V).

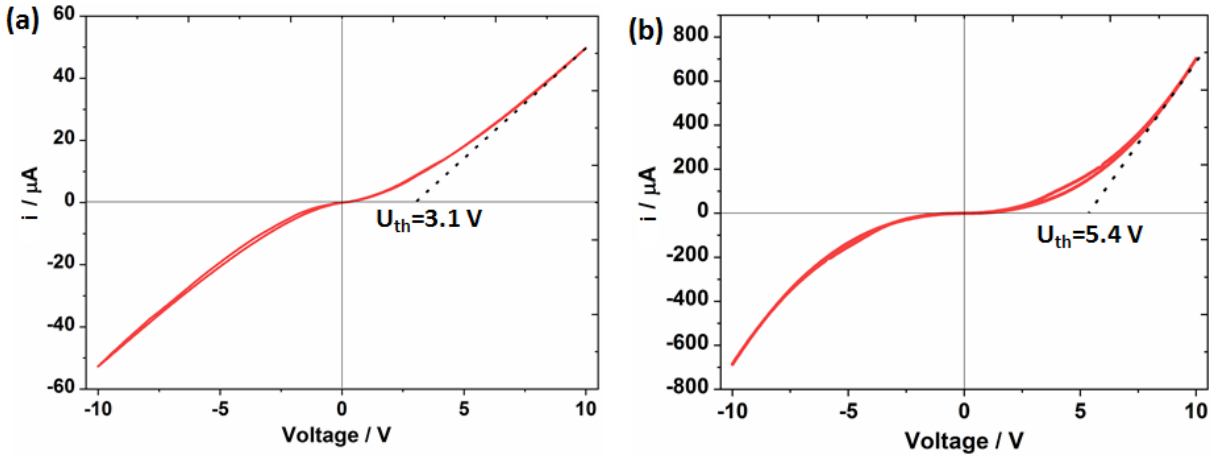

***Figure 3**: I-V curves recorded in the range of -10 V to +10 V of Cu(F_{16}Pc)/$LuPc_2$ MSDI heterojunction devices based on big electrode (a) and small electrode (b).*

To understand the different I-V profiles of the two MSDI heterojunction devices, in depth charge transport studies were performed by impedance spectroscopy. The Nyquist plots of the impedance measurements at different DC bias in the range of 0 to 10 V and at a fixed AC bias of 0.2 V are shown in Fig. 4. These plots display two depressed semicircles, in which the one at high frequency (HF) remains constant with the changing DC bias, while the one at low frequency (LF) gets smaller with increasing DC bias. Therefore, the semicircle at HF corresponds to the bulk charge transport, while the one at LF corresponds to interfacial charge transport in the devices [45]. However, the relative size of the each semicircle in the Nyquist plots and the impedance magnitude depend on the electrode geometry of the devices. For instance, the semicircle at HF in small electrode-based device is much smaller than the semicircle at LF (Fig. 4b), indicating a faster charge transport in the bulk of the heterostructure. Moreover, the real and imaginary impedances of the big electrode-based device (Fig. 4a) are much higher, compared to the small electrode-based device. Thus, a broader conclusion can be

drawn, as the charge transport in the heterostructure gets easier when the electrodes size and gap between them become smaller.

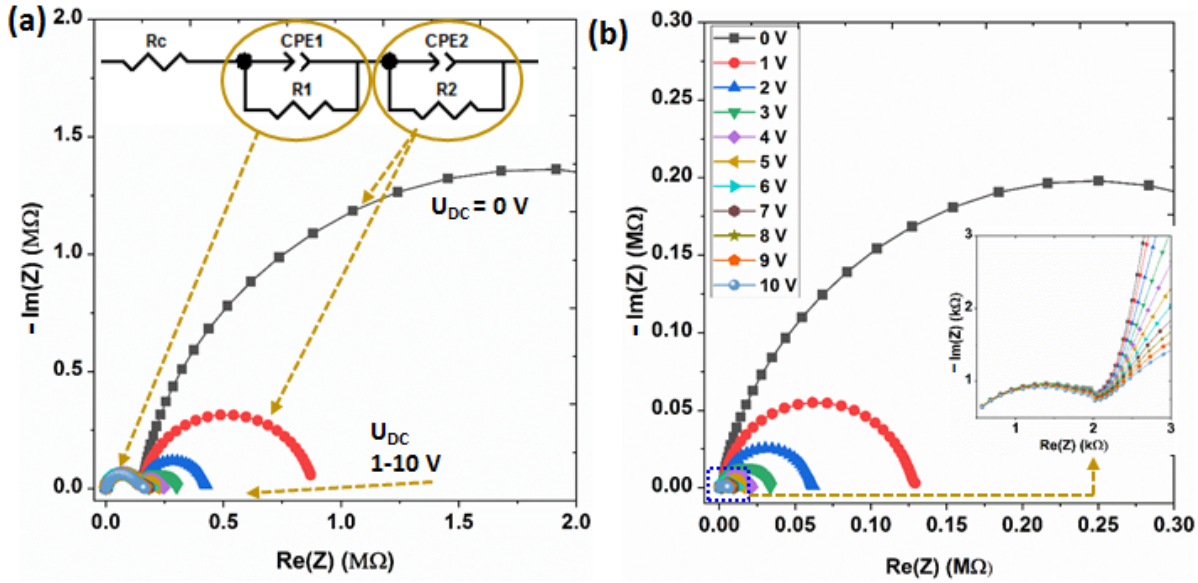

***Figure 4**: Nyquist plots of Cu(F_{16}Pc)/$LuPc_2$ MSDI heterojunction devices based on big electrode (a) and small electrode (b) recorded at different DC bias in the range of 0–10 V for a fixed AC bias 0.2 V.*

Nyquist plots were modelled by constant phase element (CPE)-based equivalent circuit, considering the distributed microstructural properties of the heterostructure [46, 47]. Different charge transport parameters such as resistance, alpha (α) and effective capacitance (C_{eff}) were determined from the modelling to predict the electrical nature of the heterojunction devices. These parameters are related to CPE and are defined according to Eq. S1 and Eq. S2 in supporting information. The experimental Nyquist plots were fitted, using two-component Ri-CPEi circuit, which are connected in series (inset of Fig. 4a). In the equivalent circuit, R1 and CPE1 describe the semicircle at HF, thus they are the charge transport parameters in the bulk of the material, while R2 and CPE2 describe the semicircle at LF, so they are the interfacial charge transport parameters. Fig. 5 depicts the variation of resistances (R1 and R2), alpha (α1 and α2) and capacitances (C_{eff1} and C_{eff2}) of big electrode (Fig. 5a, 5b and 5c) and small electrode (Fig. 5d, 5e and 5f) based devices. It is evident from Fig. 5a and 5d that R2 experiences an exponential decay, while R1 remains constant with increasing DC bias, for both

devices. It indicates that interfacial charge transport rapidly becomes faster but bulk charge transport remains constant with increasing DC bias. Moreover, the magnitude of R1 and R2 of big electrode-based device is more than 75-times and 5-times higher, respectively than the R1 and R2 of small electrode-based device, highlighting that narrow gap between the electrodes facilitates the fast charge transport in the device. Such variations in the charge transport are explained through the schemes given in Fig. 5g and 5h for the big and the small electrode-based devices, respectively. The schemes depict the accumulation of mobile charges at the interface of Cu(F_{16}Pc) and $LuPc_2$ layers, owing to their different workfunction ($\Phi_{Cu(F16Pc)}$: 5.6 eV; Φ_{LuPc2}: 5.2 eV) and the preferred charge transport pathway through the interface [26]. As the bias increases, the electric field is strengthened between the electrode and the interface. Consequently, the injected charges from the electrode can arrive at the interface more easily, enhancing the interfacial conductivity and thus decreasing the R2. However, charge transport in the bulk of Cu(F_{16}Pc) film takes place by the hopping of electrons between the discrete energy levels [48], which increases very slowly with increasing bias. Therefore, R1 of big and small electrode-based devices reveals a decrease from 148 kΩ to 126 kΩ and from 1.9 kΩ to 1.7 kΩ, respectively, as bias changes from 0 V to 10 V, which are negligible compared to the huge decrease in R2. Furthermore, relatively larger R2 of big electrode-based device is assigned to the longer interfacial pathway (75 µm) for the charge transport, compared to a shorter interfacial pathway (10 µm) present in the small electrode-based device. Notably, the narrow gap (10 µm) between the electrodes results in 75-times lower bulk resistance in the Cu(F_{16}Pc) phase, which is attributed to the localization of the electric field lines just above the electrode, sampling the area of Cu(F_{16}Pc) layer immediately above the electrode. On the other hand, when gap between the electrodes are wide (75 µm), the electric field lines are distributed in all the directions, thus sampling a large resistive area of Cu(F_{16}Pc), resulting in higher resistance [33, 49].

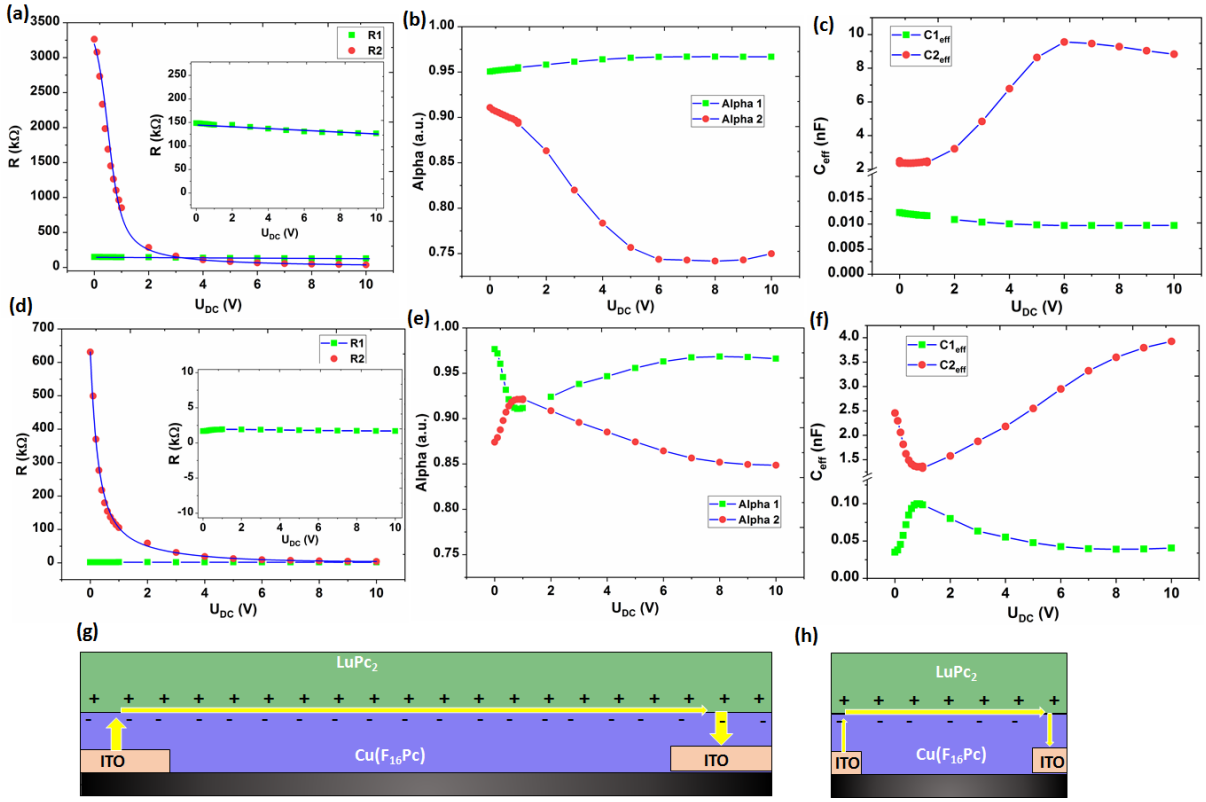

***Figure 5**: The variation of charge transport parameters; resistance (a and d), alpha (b and e) and capacitance (c and e) with applied DC bias in the range of 0 to 10 V of Cu(F_{16}Pc)/$LuPc_2$ MSDI heterojunction devices based on big electrode (image panels a, b and c) and on small electrode (image panels d, e and f). Schemes of the charge accumulation and transport in big electrode (g) and small electrode (h) based devices.*

The α indicates heterogeneity in the R-CPE circuit, such that a value of 1 corresponds to a homogeneous CPE (perfect capacitor) and a decrease towards zero means increase in heterogeneity of the CPE (perfect resistor at α = 0). The α1 of both devices are more than 0.91, and increases up to 0.97 at higher bias (Fig. 5b and 5e), indicating that CPEs associated to bulk are highly homogeneous. This is expected because there is low dispersion in the bulk microstructural properties of Cu(F_{16}Pc) layer. On the contrary, α2 decreases with increasing bias, such that a rapid decrease from 0.91 to 0.74 is noticed in big electrode-based device, while a relatively slower decrease from 0.92 to 0.84 is observed in small electrode-based device. This is linked to the increase in heterogeneity in the interfacial CPEs with increasing bias. The larger

decrease in α2 of big electrode-based device is attributed to the wide gap between the electrodes, imparting a longer interface region in the charge transport pathway. The increase of the interfacial area enhances the probability of dispersion in the microstructural properties, thus higher heterogeneity in the CPE is expected. The change in the capacitances of the devices were assessed to understand the interfacial charges accumulation and their variation with the bias and the electrode geometries. From the Fig. 5c and 5f, it is evident that C_{eff2} is much higher than the C_{eff1} for both devices, which infers that interfacial capacitance in the heterojunction devices are higher than the bulk capacitance. Considering that capacitance is inversely proportional to the layer thickness, the interface region is much thinner than the bulk of the heterostructure, which is a characteristic feature of organic heterojunction effect [17]. Thus, it further corroborates the interfacial accumulation of mobile charges in Cu(F_{16}Pc)/$LuPc_2$ heterostructure and validity of the charge transport schemes in Fig. 5g and 5h. The increase of C_{eff2} as a function of increasing bias is commensurate with the arrival of more charges at the interface as a consequence of effective overcoming of the interfacial energy barrier. The relatively higher interfacial capacitance in the big electrode-based device is assigned to the larger interfacial area, owing to the wider gap between the electrodes.

3.3. Ammonia sensing properties

The ammonia sensing properties of the heterojunction devices were investigated at first by performing successive alternate long exposure for 10 min to 90 ppm of NH_3 and recovery under clean air for 15 min at different applied bias in the range of 0.25 to 5 V. The response curves (Fig. 6) reveal a current increase upon NH_3 exposure and a current decrease during recovery under clean air, highlighting n-type behavior of the heterojunction devices taking into account the electron donating nature of NH_3. Such behavior is expected, owing to the presence of e^- in the conduction channels of the two devices (Fig. 5g and 5h). However, the magnitude of the current variation (Δi) and the evolution of the current-time (i-t) curves under different

exposure / recovery cycles depend on the electrode geometry and the applied bias. For instance, Δi for small electrode-based device is higher than those for big electrode-based device at all the applied bias. Moreover, the evolution of the Δi profiles are different for the two sensing devices. The big electrode-based device exhibits a slow increase at low bias (up to 1 V) followed by a plateau between 1 and 3 V and a fast increase at higher bias (Fig. 6c). On the other hand, the small electrode-based device experienced slow linear increase at low bias (zoomed image in Fig. S3), followed by an exponential rise at higher bias (Fig. 6f). Different Δi profiles as a function of the bias indicate that interaction of NH_3 on the sensing surface is different in the two sensors. The interaction of NH_3 with the sensing layer involves an interplay of surface adsorption followed by charge transfer and bulk diffusion [37], in which the former is a rapid and reversible process, while the latter is a relatively slower event. Both of these processes operate simultaneously, but the predominance of either of the two determines the shape of the steady-state current transient of the i-t curves. A plateau in the i-t curves at low bias (Fig. 6a and 6d) during the exposure steps indicates that NH_3 interaction on the sensing layer is diffusion limited (dominant surface adsorption and faster charge transfer). On the contrary, lack of any plateau in the i-t curves at higher bias of both the sensing devices evidences that NH_3 interaction is reaction limited and diffusion is very fast within the sensing film. Moreover, when the bulk diffusion contribution is low, NH_3 adsorption and follow-up charge transfer are mainly confined to the sensor top surface, involving only a tiny fraction of the total available active sites in the sensing film. It explains the slow increase or a plateau like behavior in Δi profiles in Fig. 6c and 6f at lower bias. On the other hand, when diffusion is predominant, NH_3 interacts with the active sites within the volume of the sensing film, causing an exponential rise in the Δi at higher bias. Notably, the diffusion of NH_3 within the sensing layer is more dominant in the small electrode-based device, which is clearly demonstrated in the ratio of Δi versus bias plot (Fig. S4). The plot displays that Δi under NH_3 exposure is ca. 7-times and ca. 200-times higher in

lower bias up to 1 V and at higher bias of 4 and 5 V, respectively, for small electrode-based device than that of big electrode-based device.

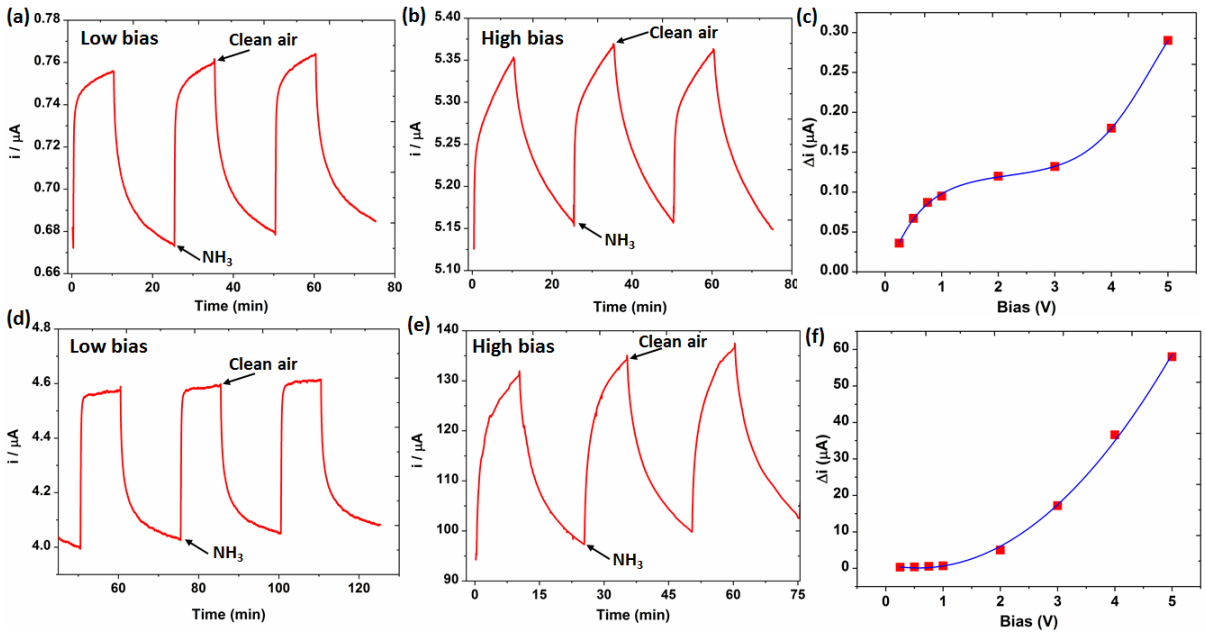

***Figure 6**: Response curves obtained at 3 successive alternate exposures to 90 ppm of NH_3 (10 min) and recovery under clean air (15 min) of Cu(F_{16}Pc)/$LuPc_2$ MSDI heterojunction devices with big electrode (a and b) and small electrode (d and e). The applied bias are 0.75 V and 4 V for the response curves in (a and d) and (b and e), respectively. The variations of current upon NH_3 exposure with applied bias for big electrode (c) and small electrode (f) based devices. Room temperature working condition (20–22°C) and fixed RH of 40%.*

The different kinetics of surface adsorption and bulk diffusion with changing bias in both the sensing devices are further analyzed by the evolution of response time ($t_{response}$) and recovery time ($t_{recovery}$) with applied bias (Fig. S5). The $t_{response}$ and $t_{recovery}$ are shorter at lower bias, while they are longer at higher bias. Moreover, the sensor with small electrodes displayed faster response ($t_{response}$ ~ 30 s) and recovery kinetics than the sensor with big electrode ($t_{response}$ ~ 180 s) in the low bias regime, demonstrating an important role played by the electrode geometry on the sensor performances. Considering the faster response/recovery kinetics and stable responses of the sensors at lower bias, sensing performances were further assessed in a wide NH_3 concentration range from 10 to 90 ppm through short exposure/recovery steps of 1

min/4 min at an applied bias of 0.5 V. The response curves of the sensors (Fig. 7) exhibit stable baseline and reversible variations of current during the exposure and recovery steps. Moreover, the sensors responses are repeatable at each concentration level, demonstrated by the similar variations of current at all five consecutive exposure/recovery cycles. Notably, the sensor with small electrode shows more than 8-times higher Δi at different concentrations of NH_3, compared to the big electrode-based sensor, highlighting the higher sensitivity of the former in a wide NH_3 concentration range. From the sensors response curves, the relative response (RR) was calculated by equation 1, in which I_{NH3} and I_{air} are the sensor current at the end of the exposure and the recovery cycles, respectively.

$$RR\ (\%) = \frac{I_{NH_3} - I_{air}}{I_{air}} \times 100 \qquad (1)$$

The calibration curves of the two sensors, depicting the evolution of RR as a function of NH_3 concentration have been compared in Fig. 7c. At first, it can be remarked that the RR of small electrode-based sensor increases from 5% to 17%, while the RR of big electrode-based sensor increases from 3% to 9%, when NH_3 concentration increases from 10 ppm to 90 ppm. Moreover, the RR of small electrode-based sensor are higher at all NH_3 concentrations, compared to the big electrode-based sensor. Therefore, the small electrode-based device is a better ammonia sensor in the studied concentration range. Notably, the calibration curves are not linear for both the sensors and the rate of increase in the RR experiences an exponential decay with increasing NH_3 concentrations. Such behavior of the sensors is attributed to the limited number of available active sites on the sensors surface, which tend to saturate with increasing ammonia concentrations [47].

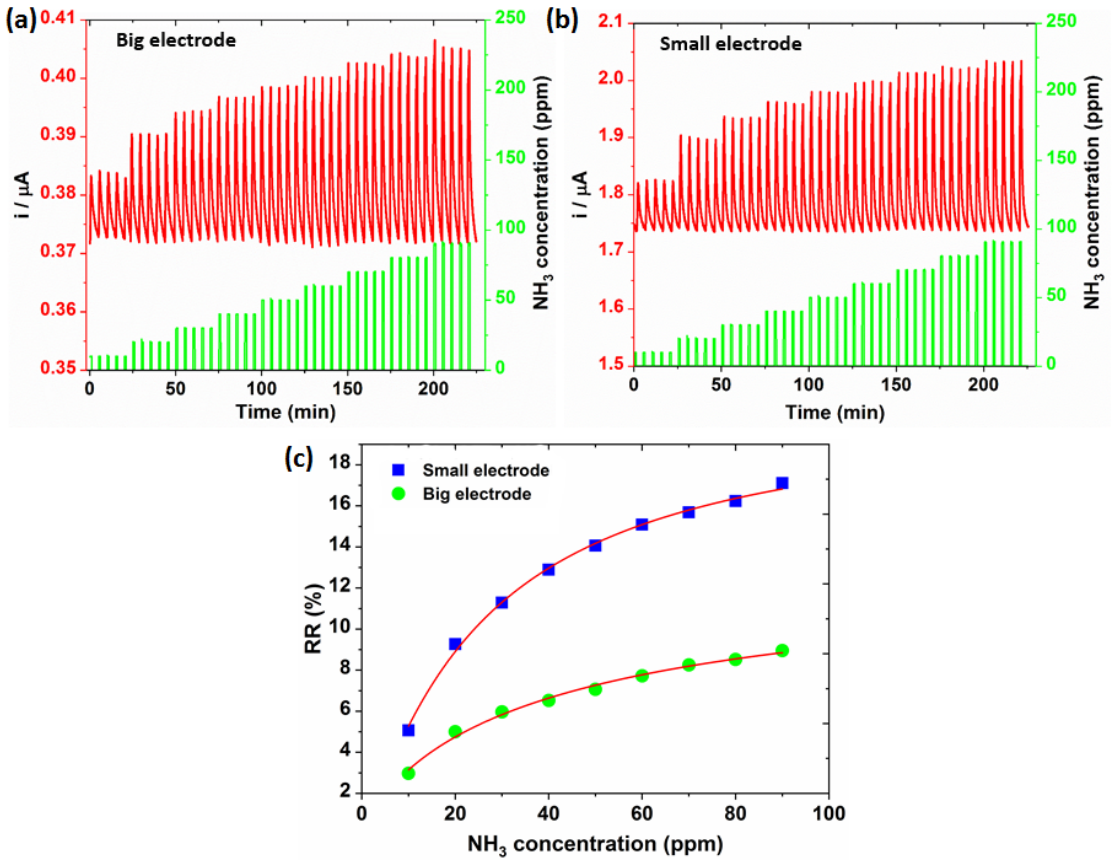

***Figure 7**: Response curves of Cu(F_{16}Pc)/LuPc_2 MSDI heterojunction devices based on big electrode (a) and small electrode (b) at short exposure / recovery steps of 1 min / 4 min at a fixed RH of 40% and applied bias of 0.5 V. The variations of RR with NH_3 concentration in the range of 10 to 90 ppm for the two sensors (c). Room temperature working condition (20–22°C).*

Humidity is a potential interferent in the selective detection of NH_3 in real environment condition. Therefore, performances of the sensors to different NH_3 concentrations were investigated in a broad range of RH (10–70%). The response curves of the sensors exhibit reversible and repeatable variations of the current during consecutive exposure/recovery cycles at each studied concentration of NH_3 and a stable baseline at a fixed RH level (Fig. 8a and 8b). However, the sensors baselines change with the variation of RH, especially at the higher RH (70%) in the small electrode-based sensor and at lower RH (10%) in the big electrode-based sensor. To further assess the interference of RH variations on the response of the sensors, RR of the sensors were estimated and are plotted as a function of RH (Fig. 8c and 8d).

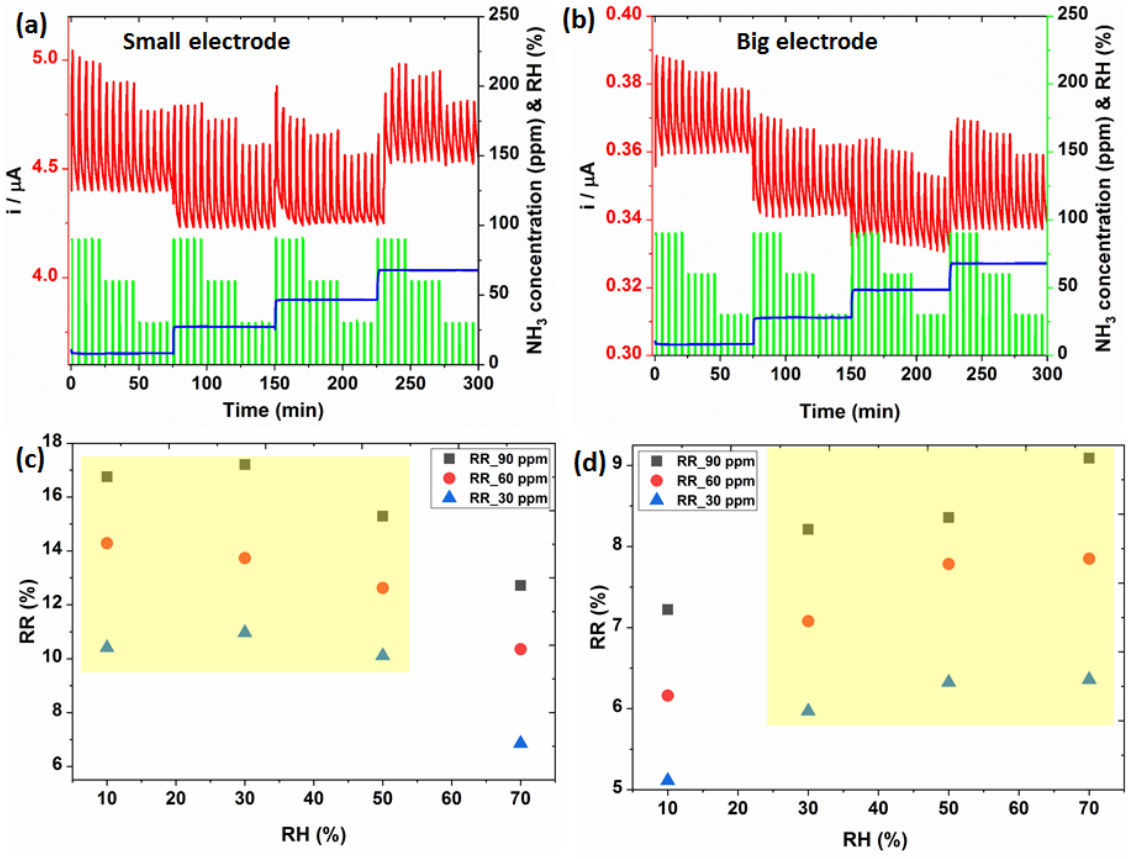

***Figure 8**: Response curves of Cu(F_{16}Pc)/$LuPc_2$ MSDI heterojunction devices based on small electrode (a) and big electrode (b) at three different ammonia concentrations (30, 60 and 90 ppm), during short exposure/recovery cycles (1 min/4 min) in the RH range of 10 to 70% and an an applied bias of 0.5 V. The variations of RR of the small electrode (c) and the big electrode (d) based sensors at three different ammonia concentrations (30, 60 and 90 ppm) with RH change in the range of 10 to 70%. Room temperature working condition (20–22°C).*

Two contrasting features are observed for the big electrode and the small electrode-based sensors. The RR of the big electrode-based sensor at different NH_3 concentrations increases with increasing RH from 10 to 70%, while an opposite behavior is noted in the small electrode-based sensor. We can explain this behavior considering the adsorption dynamics of water vapor with changing RH and surface morphology. The adsorption of water molecule on solid surface is complex phenomenon. It was reported previously that at low RH, hydrogen-bonded icelike network of water grows on a solid surface, while at higher RH, a molecular film

of water starts developing [50]. In the liquid molecular film of water, NH_3 is solvated through an acid-base reaction [51] (equation 1) , generating ammonium ion, which facilitates charge transfer in the sensing layer.

$$NH_3 + H_2O \rightarrow NH_4^+ + OH^- \qquad (1)$$

Indeed, in many chemiresistors and organic heterojunction sensors reported previously, response to NH_3 increases with increasing humidity [52, 53]**.** However, when the coverage of the sensor surface with water molecule is incomplete, the equilibrium is shifted towards ice-like water structure instead of liquid water, in which there is no dissolution of NH_3. On the contrary, water molecules compete with NH_3 to occupy an active adsorption site on the sensor surface. In this case NH_3 molecules can get adsorbed only by removing the weakly adsorbed H_2O [54]. Such competitive sorption can diminish the sensor response towards NH_3. In the present case, although the sensing material remains the same in the two sensors, but the surface morphology is different. For instance, in small electrode gap-based sensor, there are 125 digits in the interdigitated electrode assembly, while in big electrode gap-based sensor, there are 16 digits. Therefore, the surface is more rugged in small electrode-based sensor, offering larger surface for adsorption. Thus, it is expected that there is no condensation of ice-like water structure in small electrode-based sensor. Therefore, competitive sorption kinetics of H_2O and NH_3 dominates and determine the sensor response. On the other hand, less rugged surface of big electrode-based sensor undergoes faster coverage with H_2O molecules and condensation into liquid water at higher RH, facilitating charge transfer upon NH_3 dissolution. Thus, change in the RH interferes with the NH_3 sensing properties of both sensors. Nonetheless, it is worth mentioning that despite RH interference, the responses of the big electrode-based sensor at 30 ppm, 60 ppm and 90 ppm of NH_3 can be discriminated when RH change from 30% to 70%. On the other hand, responses of the small electrode-based sensor for the similar concentrations of NH_3 can be discriminated when RH change from 10% to 50%. Thus, the sensors are suitable

for selective detection of NH_3 at different concentrations in the indoor environment where RH change is limited in the range of 30–60%. However, for specific applications, in which wider RH fluctuations take place, a RH correction to the sensor's response is necessary.

Conclusions

We have demonstrated the key roles of electrode geometry and applied bias on the charge transport and NH_3 sensing performances of Cu(F_{16}Pc)/$LuPc_2$ MSDI heterojunction sensors. The bilayer heterostructure prepared by sequential deposition of Cu(F_{16}Pc) and $LuPc_2$ layers reveals a superposition of the electronic and the structural properties of each constituent. The heterojunction devices show a non-linear I-V characteristic. Further studies by impedance spectroscopy reveals 75-times faster charge transport in the bulk and 5-times faster charge transport at the interface of the small electrode-based device, compared to the big electrode-based device. Moreover, the interfacial charge transport becomes faster in both devices with increasing bias. The variation of the electrode geometry in the heterojunction devices shows a strong influence on their NH_3 sensing performances. The small electrode-based sensor shows a higher response to NH_3 and faster response kinetic than the big electrode-based sensor. Additionally, the response of each sensor increases and $t_{response}$ gets longer with increase in the bias. Such behaviors of the sensors are correlated to the different gas-material interactions, involving surface adsorption and bulk diffusion. The performances of the two sensors investigated in a wide concentration range of NH_3 and at different RH values reveal low interference from RH variations and higher sensitivity of the small electrode-based sensor.

Acknowledgements

The authors acknowledge funding through PO FEDER-FSE Bourgogne 2019/2022 (via CoMICS program) and Agence Nationale de la Recherche (ANR) through the project OUTSMART (ANR-2015-CE39-0004-03). A.K. acknowledges financial support from

MatElectroCap project (region Bourgogne Franche-Comté) and BQR program (Université de Bourgogne).

References

[1] L. Morawska, P. Thai, X. Liu, A. Asumadu-Sakyi, G. Ayoko, A. Bartonova, A. Bedini, F. Chai, B. Christensen, et al., Applications of low-cost sensing technologies for air quality monitoring and exposure assessment: How far have they gone?, Environ. Int. 116 (2018) 286-299. https://doi.org/10.1016/j.envint.2018.04.018.

[2] K. Deshmukh, T. Kovářík, S.K. Khadheer Pasha, State of the art recent progress in two dimensional MXenes based gas sensors and biosensors: A comprehensive review, Coord. Chem. Rev. 424 (2020) 213514. https://doi.org/10.1016/j.ccr.2020.213514.

[3] J. Dai, L. Li, B. Shi, Z. Li, Recent progress of self-powered respiration monitoring systems, Biosens.Bioelectron. 194 (2021) 113609. https://doi.org/10.1016/j.bios.2021.113609.

[4] A. Dey, Semiconductor metal oxide gas sensors: A review, Mater. Sci. Eng. B 229 (2018) 206-217. https://doi.org/10.1016/j.mseb.2017.12.036.

[5] S.W. Lee, W. Lee, Y. Hong, G. Lee, D.S. Yoon, Recent advances in carbon material-based NO_2 gas sensors, Sens. Actuators, B 255 (2018) 1788-1804. https://doi.org/10.1016/j.snb.2017.08.203.

[6] Y.C. Wong, B.C. Ang, A.S. Haseeb, A.A. Baharuddin, Y.H. Wong, Conducting polymers as chemiresistive gas sensing materials: A review, J. Electrochem. Soc. 167(3) (2019) 037503. https://doi.org/10.1149/2.0032003jes.

[7] R. Paolesse, S. Nardis, D. Monti, M. Stefanelli, C. Di Natale, Porphyrinoids for chemical sensor applications, Chem. Rev. 117(4) (2017) 2517-2583. https://doi.org/10.1021/acs.chemrev.6b00361.

[8] S. Das, S. Mojumder, D. Saha, M. Pal, Influence of major parameters on the sensing mechanism of semiconductor metal oxide based chemiresistive gas sensors: A review focused on personalized healthcare, Sens. Actuators, B 352 (2022) 131066. https://doi.org/10.1016/j.snb.2021.131066.

[9] T. Tung, M. Tran, J.-F. Feller, M. Castro, T. Van Ngo, K. Hassan, M.J. Nine, D. Losic, Graphene and metal organic frameworks (MOFs) hybridization for tunable chemoresistive sensors for detection of volatile organic compounds (VOCs) biomarkers, Carbon 159 (2020) 333-344. https://doi.org/10.1016/j.carbon.2019.12.010.

[10] M. Bouvet, Chapter 5 - Hybrid and 2D nanomaterials, in: E. Llobet (Ed.), Advanced nanomaterials for inexpensive gas microsensors, Elsevier 2020, pp. 85-102. https://doi.org/10.1016/B978-0-12-814827-3.00005-0.

[11] B. Mondal, P.K. Gogoi, Nanoscale heterostructured materials based on metal oxides for a chemiresistive gas sensor, ACS Appl. Electron. Mater. 4(1) (2022) 59-86. https://doi.org/10.1021/acsaelm.1c00841.

[12] D. Zappa, V. Galstyan, N. Kaur, H.M.M. Munasinghe Arachchige, O. Sisman, E. Comini, "Metal oxide -based heterostructures for gas sensors"- A review, Anal. Chim. Acta 1039 (2018) 1-23. https://doi.org/10.1016/j.aca.2018.09.020.

[13] P. Cao, Y. Cai, D. Pawar, S.T. Navale, C.N. Rao, S. Han, W. Xu, M. Fang, X. Liu, Y. Zeng, W. Liu, D. Zhu, Y. Lu, Down to ppb level NO_2 detection by ZnO/rGO heterojunction based chemiresistive sensors, Chem. Eng. J. 401 (2020) 125491. https://doi.org/10.1016/j.cej.2020.125491.

[14] T. He, W. Liu, T. Lv, M. Ma, Z. Liu, A. Vasiliev, X. Li, MXene/SnO_2 heterojunction based chemical gas sensors, Sens. Actuators, B 329 (2021) 129275. https://doi.org/10.1016/j.snb.2020.129275.

[15] H. Tai, Z. Duan, Z. He, X. Li, J. Xu, B. Liu, Y. Jiang, Enhanced ammonia response of Ti_3C_2Tx nanosheets supported by TiO_2 nanoparticles at room temperature, Sens. Actuators, B 298 (2019) 126874. https://doi.org/10.1016/j.snb.2019.126874.

[16] A. Kumar, R. Meunier-Prest, M. Bouvet, Organic heterojunction devices based on phthalocyanines: A new approach to gas chemosensing, Sensors 20(17) (2020) 4700. https://doi.org/10.3390/s20174700.

[17] K.M. Lau, J.X. Tang, H.Y. Sun, C.S. Lee, S.T. Lee, D. Yan, Interfacial electronic structure of copper phthalocyanine and copper hexadecafluorophthalocyanine studied by photoemission, Appl. Phys. Lett. 88(17) (2006) 173513. https://doi.org/10.1063/1.2198484.

[18] H. Alves, A.S. Molinari, H. Xie, A.F. Morpurgo, Metallic conduction at organic charge-transfer interfaces, Nat. Mater. 7(7) (2008) 574-580. https://doi.org/10.1038/nmat2205.

[19] J.P. Meyer, D. Schlettwein, Influence of central metal and ligand system on conduction type and charge carrier transport in phthalocyanine thin films, Adv. Mater. Opt. Electron. 6(5-6) (1996) 239-244. https://doi.org/10.1002/(SICI)1099-0712(199609)6:5/6<239::AID-AMO274>3.0.CO;2-E.

[20] H. Brinkmann, C. Kelting, S. Makarov, O. Tsaryova, G. Schnurpfeil, D. Wöhrle, D. Schlettwein, Fluorinated phthalocyanines as molecular semiconductor thin films, phys. status solidi (a) 205(3) (2008) 409-420. 10.1002/pssa.200723391.

[21] R. Murdey, N. Sato, M. Bouvet, Frontier electronic structures in fluorinated copper phthalocyanine thin films studied using ultraviolet and inverse photoemission spectroscopies, Mol. Cryst. Liq. Cryst. 455(1) (2006) 211-218. https://doi.org/10.1080/15421400600698469.

[22] D. Cardenas-Morcoso, E. Vey, M. Heiderscheid, G. Frache, N.D. Boscher, Electronic and energy level engineering of directly fused porphyrin-conjugated polymers: Impact of the central metal cation, J. Mater. Chem. C 10(6) (2022) 2194-2204. https://doi.org/10.1039/D1TC05452J.

[23] X. Wang, S. Ji, H. Wang, D. Yan, Highly sensitive gas sensor enhanced by tuning the surface potential, Org. Electron. 12(12) (2011) 2230-2235. https://doi.org/10.1016/j.orgel.2011.09.014.

[24] S. Ji, H. Wang, T. Wang, D. Yan, A high-performance room-temperature NO_2 sensor based on an ultrathin heterojunction film, Adv. Mater. 25(12) (2013) 1755-1760. https://doi.org/10.1002/adma.201204134.

[25] V. Parra M. Bouvet, Semiconductor tranducer and its use in a sensor for detecting electron-donor or electron-acceptor species, US Patent 8450725B2, CNRS, Sorbonne Universite, France, 2013. https://patents.google.com/patent/US8450725.

[26] S. Ouedraogo, R. Meunier-Prest, A. Kumar, M. Bayo-Bangoura, M. Bouvet, Modulating the electrical properties of organic heterojunction devices based on phthalocyanines for ambipolar sensors, ACS Sensors 5(6) (2020) 1849-1857. https://doi.org/10.1021/acssensors.0c00877.

[27] Z. Şahin, R. Meunier-Prest, F. Dumoulin, A. Kumar, Ü. Isci, M. Bouvet, Tuning of organic heterojunction conductivity by the substituents' electronic effects in phthalocyanines for ambipolar gas sensors, Sens. Actuators, B 332 (2021) 129505. https://doi.org/10.1016/j.snb.2021.129505.

[28] A. Wannebroucq, G. Gruntz, J.-M. Suisse, Y. Nicolas, R. Meunier-Prest, M. Mateos, T. Toupance, M. Bouvet, New n-type molecular semiconductor–doped insulator (MSDI) heterojunctions combining a triphenodioxazine (TPDO) and the lutetium bisphthalocyanine ($LuPc_2$) for ammonia sensing, Sens. Actuators, B 255 (2018) 1694-1700. https://doi.org/10.1016/j.snb.2017.08.184.

[29] P. Gaudillat, A. Wannebroucq, J.-M. Suisse, M. Bouvet, Bias and humidity effects on the ammonia sensing of perylene derivative/lutetium bisphthalocyanine MSDI heterojunctions, Sens. Actuators, B 222 (2016) 910-917. https://doi.org/10.1016/j.snb.2015.09.015.

[30] M. Bouvet, Radical phthalocyanines and intrinsic semiconduction, in: K.M. Kadish, K.M. Smith, R. Guilard (Eds.), The Porphyrin Handbook, Academic Press, Amsterdam, 2003, pp. 37-103. https://doi.org/10.1016/B978-0-08-092393-2.50008-1.

[31] G. Bengasi, R. Meunier-Prest, K. Baba, A. Kumar, A.L. Pellegrino, N.D. Boscher, M. Bouvet, Molecular engineering of porphyrin-tapes/phthalocyanine heterojunctions for a highly sensitive ammonia sensor, Adv. Electron. Mater. 6(12) (2020) 2000812. https://doi.org/10.1002/aelm.202000812.

[32] S.P. Lee, Electrodes for semiconductor gas sensors, Sensors 17(4) (2017). https://doi.org/10.3390/s17040683.

[33] D.E. Williams, K.F.E. Pratt, Theory of self-diagnostic sensor array devices using gas-sensitive resistors, J. Chem. Soc., Faraday Trans. 91(13) (1995) 1961-1966. https://doi.org/10.1039/FT9959101961.

[34] N.M. Shaalan, T. Yamazaki, T. Kikuta, Effect of micro-electrode geometry on NO_2 gas-sensing characteristics of one-dimensional tin dioxide nanostructure microsensors, Sens. Actuators, B 156(2) (2011) 784-790. https://doi.org/10.1016/j.snb.2011.02.039.

[35] J.W. Gardner, Intelligent gas sensing using an integrated sensor pair, Sens. Actuators, B 27(1) (1995) 261-266. https://doi.org/10.1016/0925-4005(94)01598-C.

[36] J. Tamaki, A. Miyaji, J. Makinodan, S. Ogura, S. Konishi, Effect of micro-gap electrode on detection of dilute NO_2 using WO_3 thin film microsensors, Sens. Actuators, B 108(1) (2005) 202-206. https://doi.org/10.1016/j.snb.2004.09.047.

[37] J.W. Gardner, M.Z. Iskandarani, B. Bott, Effect of electrode geometry on gas sensitivity of lead phthalocyanine thin films, Sens. Actuators, B 9(2) (1992) 133-142. https://doi.org/10.1016/0925-4005(92)80206-D.

[38] T. Yang, Optimizing electrode structure of carbon nanotube gas sensors for sensitivity improvement based on electric field enhancement effect of fractal geometry, Sci. Rep. 11(2021) 16675. https://doi.org/10.1038/s41598-021-96239-1

[39] G.L. Kikobo, A. Kumar, V. Vibhu, S. Ouedraogo, A. Deshotel, M. Mateos, R. Meunier-Prest, M. Bouvet, Photon assisted-inversion of majority charge carriers in molecular semiconductor-based organic heterojunctions, J. Mater. Chem. C 9(14) (2021) 5008-5020. https://doi.org/10.1039/D0TC05828A.

[40] J. Mack, M.J. Stillman, Transition assignments in the ultraviolet−visible absorption and magnetic circular dichroism spectra of phthalocyanines, Inorg. Chem. 40(4) (2001) 812-814. https://doi.org/10.1021/ic0009829.

[41] T. Basova, E. Kol'tsov, A. Hassan, A. Tsargorodskaya, A. Ray, I. Igumenov, Thin films of copper hexadecafluorophthalocyanine $CuPcF_{16}$, phys. status solidi (b) 242(4) (2005) 822-827. https://doi.org/10.1002/pssb.200460009.

[42] D. Markovitsi, T.-H. Tran-Thi, R. Even, J. Simon, Near infrared absorption spectra of lanthanide bis-phthalocyanines, Chem. Phys. Lett. 137(2) (1987) 107-112. https://doi.org/10.1016/0009-2614(87)80313-5.

[43] S. Yim, S. Heutz, T.S. Jones, Influence of intermolecular interactions on the structure of phthalocyanine layers in molecular thin film heterostructures, Phys. Rev. B 67(16) (2003) 165308. https://doi.org/10.1103/PhysRevB.67.165308.

[44] S. Yadav, P. Kumar, S. Ghosh, Optimization of surface morphology to reduce the effect of grain boundaries and contact resistance in small molecule based thin film transistors, Appl. Phys. Lett. 101(19) (2012) 193307. https://doi.org/10.1063/1.4766913.

[45] K.A. Miller, R.D. Yang, M.J. Hale, J. Park, B. Fruhberger, C.N. Colesniuc, I.K. Schuller, A.C. Kummel, W.C. Trogler, Electrode independent chemoresistive response for cobalt phthalocyanine in the space charge limited conductivity regime, J. Phys. Chem. B 110(1) (2006) 361-366. https://doi.org/10.1021/jp053104a.

[46] B. Hirschorn, M.E. Orazem, B. Tribollet, V. Vivier, I. Frateur, M. Musiani, Determination of effective capacitance and film thickness from constant-phase-element parameters, Electrochim. Acta 55(21) (2010) 6218-6227. https://doi.org/10.1016/j.electacta.2009.10.065.

[47] A. Kumar, R. Meunier-Prest, F. Herbst, O. Heintz, E. Lesniewska, M. Bouvet, Covalent grafting of aryls to modulate the electrical properties of phthalocyanine-based heterostructures: Application to ammonia sensing, Chem. Eng. J. 436 (2022) 135207. https://doi.org/10.1016/j.cej.2022.135207.

[48] J. Zaumseil, H. Sirringhaus, Electron and ambipolar transport in organic field-effect transistors, Chem. Rev. 107(4) (2007) 1296-1323. https://doi.org/10.1021/cr0501543.

[49] M.J. Toohey, Electrodes for nanodot-based gas sensors, Sens. Actuators, B 105(2) (2005) 232-250. https://doi.org/10.1016/j.snb.2004.06.006.

[50] D.B. Asay, S.H. Kim, Evolution of the adsorbed water layer structure on silicon oxide at room temperature, J. Phys. Chem. B, 109(2005) 16760-3. https://doi.org/10.1021/jp053042o

[51] B.A.J. Lechner, Y. Kim, P.J. Feibelman, G. Henkelman, H. Kang, M. Salmeron, Solvation and reaction of ammonia in molecularly thin water films, J. Phys. Chem. C, 119(2015) 23052-8. https://doi.org/10.1021/acs.jpcc.5b07525

[52] F. Rigoni, S. Freddi, S. Pagliara, G. Drera, L. Sangaletti, J.M. Suisse, et al., Humidity-enhanced sub-ppm sensitivity to ammonia of covalently functionalized single-wall carbon nanotube bundle layers, Nanotechnology, 28(2017) 255502. https://doi.org/10.1088/1361-6528/aa6da7

[53] M. Mateos, R. Meunier-Prest, J.-M. Suisse, M. Bouvet, Modulation of the organic heterojunction behavior, from electrografting to enhanced sensing properties, Sensors and Actuators B: Chemical, 299(2019) 126968. https://doi.org/10.1016/j.snb.2019.126968

[54] M. Matsuguchi, A. Okamoto, Y. Sakai, Effect of humidity on NH3 gas sensitivity of polyaniline blend films, Sensors and Actuators B: Chemical, 94(2003) 46-52. https://doi.org/10.1016/S0925-4005(03)00325-3